



## **Atomically Resolved Interfacial Analysis of Bone-Like Hydroxyapatite Nanoparticles on Titanium**

Downloaded from: <https://research.chalmers.se>, 2025-12-04 17:03 UTC

Citation for the original published paper (version of record):

Eriksson, G., Hulander, M., Thuvander, M. et al (2023). Atomically Resolved Interfacial Analysis of Bone-Like Hydroxyapatite Nanoparticles on Titanium. *Advanced NanoBiomed Research*, 3(10).  
<http://dx.doi.org/10.1002/anbr.202300051>

N.B. When citing this work, cite the original published paper.

# Atomically Resolved Interfacial Analysis of Bone-Like Hydroxyapatite Nanoparticles on Titanium

Gustav Eriksson, Mats Hulander, Mattias Thuvander, and Martin Andersson\*

Titanium is commonly used for medical devices, including osseointegrating implants, owing to its biocompatibility and mechanical properties. Nanostructuring titanium implants is known to enhance the healing process by promoting bone growth on the implant surface. Hydroxyapatite nanoparticles, resembling natural bone mineral, have been used to further improve osseointegration. While previous studies have investigated the osseointegration of titanium implants using atom probe tomography, limited research has focused on the attachment of synthetic hydroxyapatite to titanium. Herein, electron microscopy and atom probe tomography are used to reveal the assembly of synthetic hydroxyapatite nanoparticles in the titanium oxide surface. By sputter coating with chromium, a suitable matrix is formed for detailed interfacial analysis. The results demonstrate the diffusion of calcium, phosphorus, and carbon from hydroxyapatite nanoparticles into the titanium oxide surface.

of titanium may be further enhanced by manipulating the surface topography through various techniques, such as acid etching, blasting, and anodic oxidation,<sup>[6]</sup> or by coating it with a more bioactive material such as hydroxyapatite (HA).<sup>[7]</sup> HA has a chemical similarity to the mineral found in bone,<sup>[8]</sup> hence transforming the titanium oxide surface into a bone mimicking surface. There are several different procedures and techniques to deposit HA coatings on titanium including plasma spray, sputtering, pulsed-laser deposition ion beam, and sol-gel methods, among others.<sup>[9,10]</sup> Each of these methods has their own advantages and disadvantages, resulting in materials that vary in terms of their similarity to bone mineral, crystallinity, and adherence to the underlying implant

## 1. Introduction

Today, surgical insertion of medical implants, such as prosthetic joints and internal fixation devices, are routine procedures around the world, improving the health for many individuals.<sup>[1,2]</sup> Although success rates are generally high, poor tissue integration or implant associated infection can occur where high doses of intravenously administered antibiotics or revision surgery may be the only solution.<sup>[3,4]</sup>

Titanium is one of the most commonly used metals for implants, primarily because its native oxide has a natural affinity for direct binding to bone, leading to its integration through a process known as osseointegration.<sup>[5]</sup> The integration properties

surface.<sup>[11]</sup> One common cause for failed tissue integration on hydroxyapatite-coated titanium implants is delamination of the HA coating from the titanium implant.<sup>[12]</sup> The risk of delamination is associated with the thickness of the HA layer and for this reason, thinner coatings (<1 µm) are being pursued.<sup>[13]</sup>


A successful method of improving the osseointegrating property of titanium implants involves the application of hydroxyapatite nanoparticles (nanoHA) to the implant surface.<sup>[14,15]</sup> Such nanoHA has been shown to have a high resemblance to bone mineral,<sup>[16]</sup> both in regards to chemical composition, crystallinity, and size (typically 2–30 nm), demonstrating improved osseointegration without any increased risk of infection.<sup>[17]</sup>

The functional efficacy of nanoHA-coated titanium implants has been extensively demonstrated through the introduction of several clinically used products. The mechanical properties and microstructure of HA and titanium composite materials have also been previously studied.<sup>[18,19]</sup> In some material preparation processes, an intermediate phase, such as CaTiO<sub>3</sub>, has been observed, confirming chemical reactions between hydroxyapatite and titanium,<sup>[20]</sup> similar to the reaction between bone and titanium.<sup>[21]</sup>

However, the mechanistic understanding of the binding and integration of nanoHA onto a titanium substrate remains obscured, particularly at the atomic scale. Despite the potential significance of such detailed information, the challenges associated with examining the immobilization of nanoparticles onto substrates have thus far limited our understanding of the underlying processes involved. Additionally, considering that atomic-resolution studies have previously shed light on the osseointegration of the surface oxide of titanium implant

G. Eriksson, M. Hulander, M. Andersson  
Department of Chemistry and Chemical Engineering  
Chalmers University of Technology  
SE-41296 Gothenburg, Sweden  
E-mail: martin.andersson@chalmers.se

M. Thuvander  
Department of Physics  
Chalmers University of Technology  
SE-41296 Gothenburg, Sweden

 The ORCID identification number(s) for the author(s) of this article can be found under <https://doi.org/10.1002/anbr.202300051>.

© 2023 The Authors. Advanced NanoBiomed Research published by Wiley-VCH GmbH. This is an open access article under the terms of the Creative Commons Attribution License, which permits use, distribution and reproduction in any medium, provided the original work is properly cited.

DOI: 10.1002/anbr.202300051

materials and how bone grows onto an implant during the healing process,<sup>[22,23]</sup> it is of great interest to compare this natural interface with that of pre-engineered bone-mimicking nanoHA on titanium.

Atom probe tomography, APT, is an analytical technique that provides information about the elemental composition of a material at a subnanometer, near-atomic, resolution with ppm detection sensitivity across the entire periodic table.<sup>[24]</sup> Field evaporation occurs when atoms or molecules are evaporated from a needle-shaped specimen, which is cryogenically cooled under ultrahigh vacuum and subjected to a sufficiently strong electric field. During this process, the atoms from the specimen become ionized and are accelerated toward a position sensitive detector. The measured time of flight and detection coordinates are used to sort the collected data into a mass spectrum and a 3D reconstruction of the specimen, where the chemical composition is visualized throughout the analyzed volume of the material. Recent instrumental advancements, particularly the introduction of laser-assisted APT, have expanded the application of this technique to a broader range of materials, including biominerals, bone tissue, and tooth enamel.<sup>[25]</sup> APT has also been increasingly used to study nanoparticles and a number of strategies has been attempted to establish methodologies for high throughput analysis of such materials.<sup>[26]</sup> For example, hydroxyapatite nanoparticles have successfully been studied using APT by embedding the particles in alumina and gold matrixes.<sup>[27]</sup> However, studying interfaces, especially those composed of materials with different evaporation fields, poses a significant challenge in APT, necessitating the development of novel methodologies and sample preparation techniques.

Herein, we demonstrate the use of APT to obtain a 3D reconstruction of a titanium implant surface modified with hydroxyapatite nanoparticles. This was accomplished by implementing a technique utilizing chromium sputtering embedding. Our previous studies have successfully employed APT to examine the interface between titanium and bone, both in early healing stages in rat bone<sup>[22]</sup> and after long-term clinical use in humans.<sup>[23]</sup> Comparative analysis between the bone tissue grown onto the titanium surface oxide and the predeposited synthetic hydroxyapatite and titanium will provide further insights into how surface modifications can enhance integration and accelerate the healing process.

## 2. Experimental Section

### 2.1. Material Assembly

Hydroxyapatite nanoparticle-coated titanium samples (nanoHA) were provided by Promimic AB. The samples were prepared by spin coating a calcium phosphate dispersion onto pure titanium disks, followed by incubation in room temperature and sintering at 450 °C in air for 5 min. The topography of the nanoparticle-covered surfaces was imaged using scanning electron microscopy (SEM) using a Zeiss LEO Ultra 55 operating at 5 kV, using an in-lens detector, to assess the degree of particle coverage.

Prior to APT and transmission electron microscopy (TEM) specimen preparation, the samples were covered with a 120 nm chromium film using a Leica EM ACE600 sputter coater

equipped with a chromium target. The chromium layer fills the dual purpose of forming a matrix for the hydroxyapatite nanoparticles as well as protecting the sample from damage caused by the gallium ion milling during sample preparation.<sup>[28]</sup>

### 2.2. APT and TEM Sample Preparation

APT and TEM specimens were prepared according to the standardized protocols using a dual-beam focused ion beam (FIB)/SEM system FEI Versa 3D,<sup>[29–31]</sup> with a mono-isotopic Ga (69 amu) source. The lift-out procedure for preparation of APT specimen is illustrated in **Figure 1**. A protective platinum strip was deposited using the instrument's gas injection system over the region of interest, followed by FIB milling of trenches using an acceleration voltage of the ion beam of 30 kV and a current of 5 nA surrounding the area to be lifted out. An Omniprobe micromanipulator was attached to the lift-out sample using Pt deposition and the cantilever-shaped lift-out sample was cut loose. The lift-out was placed in segments on posts on a premanufactured silicon flat-top coupon (Cameca Scientific Instruments). The sharpening of the eventual APT specimens into needles with an apex diameter below 100 nm was conducted by annular milling with the specimen parallel to the ion beam. The annular milling was performed using a circular pattern, starting with an outer and inner diameter of 6 and 3  $\mu\text{m}$ , respectively, at 30 kV and 1 nA. Gradually, the diameter of the milling pattern and the current of the ion beam were reduced. Eventually, the acceleration voltage was reduced to 5 kV and the final milling was carried out without an inner diameter at 48 pA until the protective Pt layer was removed. The final polishing of the specimen to get an as small as possible tip radius was carried out at 7.7 pA. The specimen was cleaned to remove embedded Ga with the ion beam at 2 kV and 4.3 pA.

### 2.3. TEM Analysis

TEM specimens were analyzed using an FEI Titan 80-300 operating at 300 kV and imaged in TEM mode. High-angle annular dark-field scanning TEM (HAADF-STEM) mode was used for energy-dispersive X-ray spectroscopy (EDX) analysis with an Oxford X-sight EDS detector. The EDX data were analyzed using FEI TEM Imaging and Analysis Offline version 4.7. EDX quantification was done standardless without any correction mode enabled.

### 2.4. APT Analysis

APT specimens were analyzed in a LEAP 5000 XS (CAMECA Scientific Instruments) in laser pulsing mode with the wavelength  $\lambda = 355$  nm between 65 and 95 pJ, calculated as to achieve an effective pulse fraction of approximately 25% by a procedure described by Kelly et al.<sup>[32]</sup> The temperature was set to 60 K and a detection rate at 1–2% was used.

The acquired raw APT data were reconstructed using the tip profile with the Cameca IVAS 3.6.12 software. The SEM micrographs used to obtain the tip profiles can be found in Figure S2 and S3, Supporting Information. The reconstructed 3D datasets were analyzed using Cameca IVAS 3.6.8.

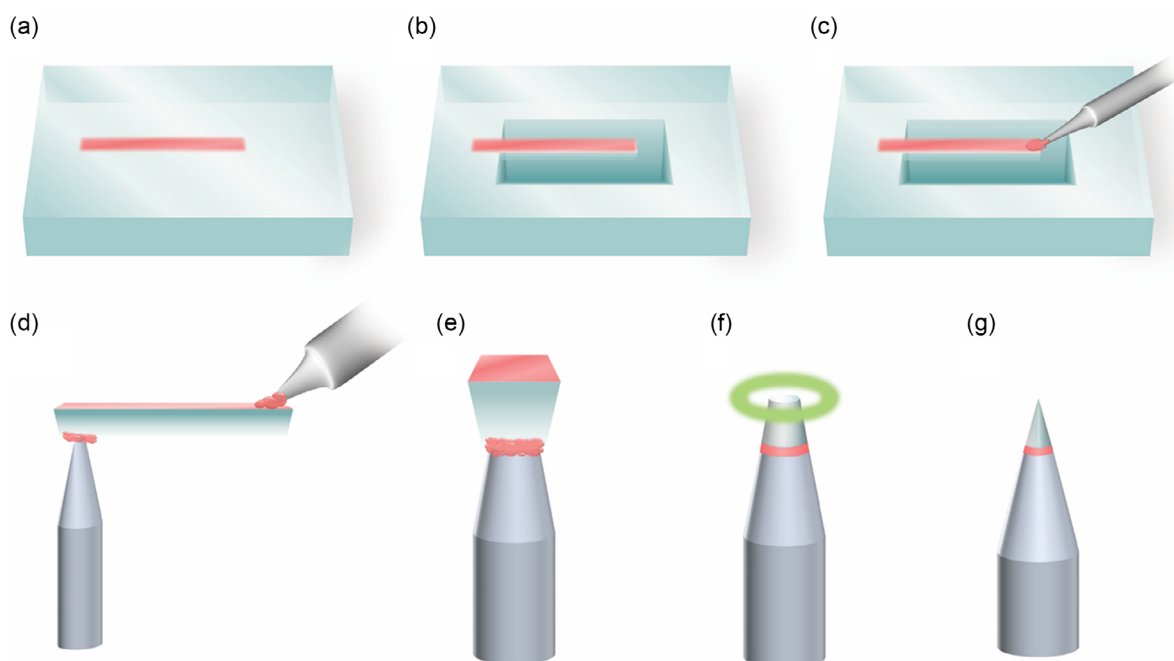


**Figure 1.** APT specimen preparation process using FIB/SEM. a) A  $2 \times 20 \mu\text{m}$  protective platinum strip deposited over a region of interest. b) Trenches milled surrounding cantilever to be lifted out. c) Micromanipulator attached to cantilever by Pt deposition. d) Liftout placed on flat-top posts using Pt deposition. e) Lift-out cut loose from flat-top post by ion milling. f) Sharpening of specimen using annular ion milling. g) Final specimen.

### 3. Results and Discussion

The surface coverage of nanoHA deposited from the dispersion onto the titanium surfaces can be observed in the SEM micrographs shown in **Figure 2**. The hydroxyapatite nature of these nanoparticles was verified with XRD, as shown in Figure S1, Supporting Information. The surface was covered to a high degree with elongated nanoparticles, stacked on each other in a mesh-like pattern. While the thickness of the particle layer was hard to estimate from these top view images, the underlying substrate was visible underneath the particles in Figure 2b.

Following the chromium sputtering and FIB/SEM sample preparation, lift-outs from the material were analyzed by TEM. An overview of the region of interest around the sample surface

can be seen in **Figure 3a**. In the close-up view, shown in Figure 3b, the nanoHA can be seen as a brighter region due to the relatively lower electron scattering compared to the surrounding chromium and titanium. While individual particles are difficult to discern, the layer of mineralized particles is clearly visible. In imaged regions where the layer appears to be one nanoparticle thick, as to the right in Figure 3b, the thickness of the layers and consequently one hydroxyapatite particle seems to be around 10–15 nm. In other regions, several particles appear to be stacked on top of each other, as can be seen at the left-hand side in Figure 3b and in the SEM images in Figure 1, causing the thickness of the hydroxyapatite layer to be larger. The titanium oxide layer on the surface can also be seen just underneath the hydroxyapatite with a measured thickness of approximately 10 nm.

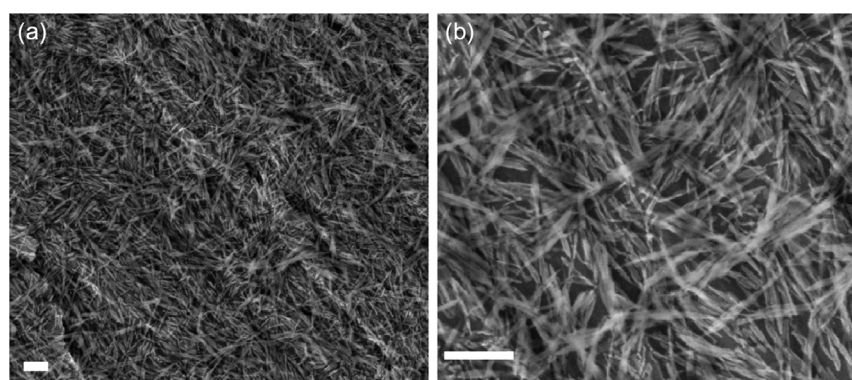


**Figure 2.** SEM micrographs of deposited hydroxyapatite nanorods on a titanium substrate. The micrograph in a) is obtained at  $50,000\times$  magnification and in b) at  $150,000\times$  magnification. Scale bars: 200 nm.



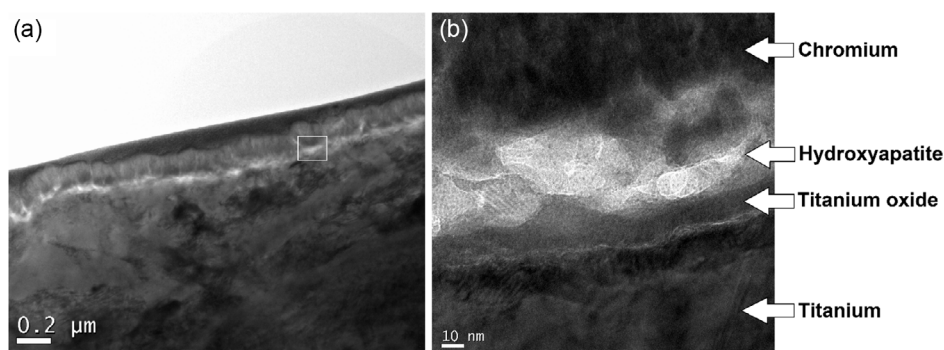


**Figure 3.** TEM micrographs of a lift-out made from a nanoHA-modified titanium substrate. The surface is covered with a sputter-coated protective chromium layer and a platinum layer deposited using a gas injection system during sample preparation. The box in image a) highlights the region magnified in image b).

The chromium layer deposited by sputter coating appears to cover the surface well and no voids are visible in the TEM micrographs.

By collecting the characteristic X-rays generated in HAADF-STEM mode, the chemical composition of the different layers was obtained. In dark field, the hydroxyapatite region appears darker than the surrounding chromium and titanium, due to the lower amount of scattered incident electrons by calcium and phosphorous. In **Figure 4**, the HAADF-STEM micrographs can be seen and in **Figure 5**, the collected EDX spectra from the regions labeled 1 and 2 in **Figure 4b** are shown. EDX spectra collected from additional areas in **Figure 4b** can be found in **Figure S5–S10**, Supporting Information, and the calculated atomic % from the X-ray spectra collected in the different regions of the sample is presented in **Table S1**, Supporting Information.

In **Figure 5**, it can be observed that some X-rays characteristics for calcium and phosphorous are collected from the titanium oxide region, suggesting that some of the atoms from the hydroxyapatite material have diffused into the oxide. However, it should be noted that the oxide and particles are in close vicinity of each other and that the X-rays collected therefore can originate from the particles. In the particle region, a large amount of chromium was detected, indicating that the space between the particles in the open mesh-like structure has been filled with chromium during sputter coating. In the chromium layer and titanium substrate, only small traces of Ca and P, if any, could be detected (**Figure S5** and **S10**, Supporting Information,

respectively). Carbon was detected around the nanoHA, which is expected because hydroxyapatite particles prepared from solution often are carbonated.<sup>[33]</sup> However, this does not necessarily explain all the detected carbon. The carbon can also be attributed to contaminations at the interface or EDX being less reliable when measuring low atomic weight elements. The detected copper is originating from the grid that the lift-out sample is placed on, and the silicon is likely originating from the detector. In the EDX spectra, a Ga signal is also detected, which is attributed to the FIB-based sample preparation.

Four APT specimens were analyzed, which all showed consistent results. None of the analyzed specimens failed by fracture, which is attributed to the matching fields of chromium and titanium<sup>[34]</sup> and good adhesion between the layers in the structure. At the interface between the sputter-coated chromium layer and the titanium surface oxide, the hydroxyapatite region was identified, as shown in **Figure 6**. Both the chromium and titanium layers were oxidized, which in conjunction with the isotopic distribution of the two elements caused the mass spectrum of the analyzed specimen to contain many peaks. Despite this, the hydroxyapatite particles on the titanium surface could be identified by the CaP peak at 71 Da, which could not be attributed to any chromium- or titanium-related ions.

The chemical composition in the protective chromium film, the titanium oxide layer, and the titanium was investigated. From this, the content of Ca and P could be assessed by analysis of the mass spectrum for the content inside the boxes shown in

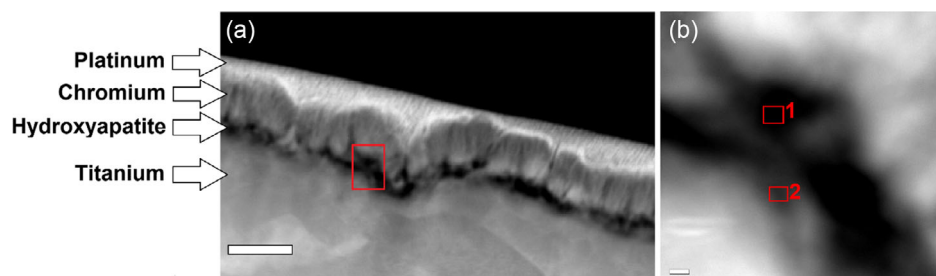


**Figure 4.** HAADF-STEM micrograph of the sample studied. a) Overview of the sample, the red box highlights the region magnified in (b). Scale bar: 200 nm. b) The region surrounding the sample surface with hydroxyapatite particles. The boxes 1 and 2 indicate the areas from which characteristic X-rays were collected for EDX analysis. Scale bar: 10 nm.

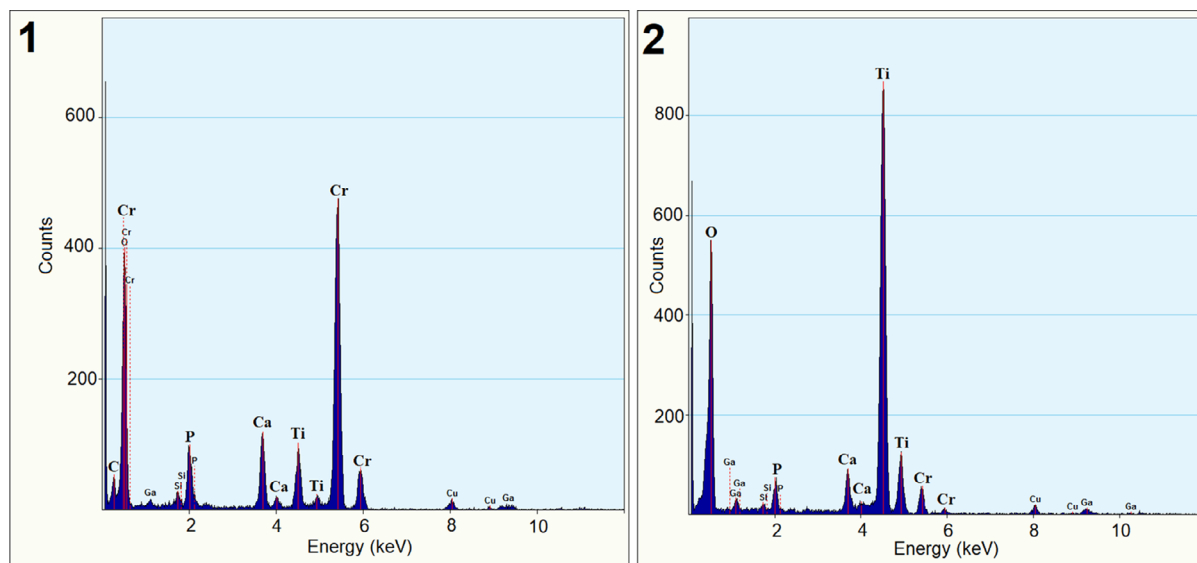


**Figure 5.** EDX spectra collected from the regions labeled as 1,2) in Figure 4b. The spectra collected in region (1) show clear calcium and phosphorous signals from the nanoHA particles embedded in chromium. The spectra collected in region (2) show calcium and phosphorous signals from the titanium surface oxide beneath the chromium embedded nanoHA.

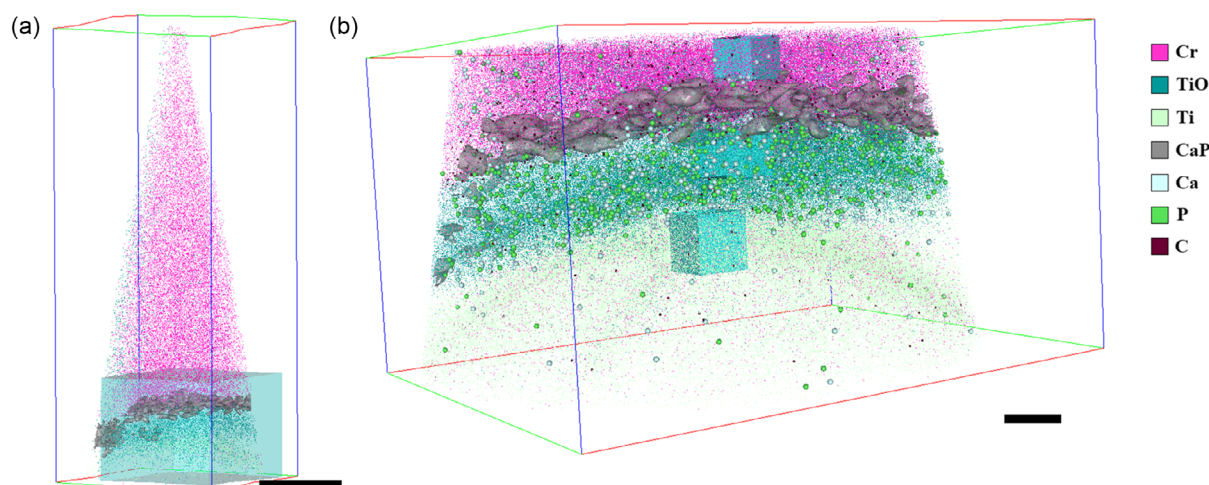


**Figure 6.** a) APT reconstruction of a full analysis of a specimen. Chromium appears as pink, titanium oxide as cyan, and titanium as green. An isosurface set at 1.75% CaP (71 Da) is in gray. Scale bar: 50 nm. b) Analysis of the region highlighted with a box in (a). The three sub-boxes were used to analyze the composition of the chromium, titanium oxide, and titanium, respectively. Scale bar: 10 nm. The species highlighted as Ca is the  $\text{CaO}_3^{2+}$  peak at 44 Da and the species highlighted as P is the  $\text{PO}_3\text{H}_2^{2+}$  peak at 40.5 Da.

Figure 6b. The mass spectra can be found in Figure S11, Supporting Information. The peaks in the mass spectra needed to be identified separately for the three regions due to overlaps of the various species that appear. The results from the mass spectrum analyses are presented in **Table 1**.

In the analyzed subvolume of titanium oxide, the Ca content was found to be 0.3% and the P content to be 0.2%. In the corresponding volume in the chromium region, the Ca content was 0.2% and the P content 0.1%. It is likely that some Ca and P are lost due to overlapping regions in the mass spectrum. For example, at 81 Da there is a possible overlap of  $\text{TiO}_2^+$  and  $\text{PO}_3\text{H}_2^+$ , as the signal is higher than what would be expected based on the

**Table 1.** Measured bulk composition (atomic %) of the different regions highlighted in Figure 6b, obtained by mass spectrum analysis of the reconstructed APT data.

Region	Cr	Ti	O	Ca	P	C	H <sup>a)</sup>
Chromium	75	–	24	0.2	0.1	0.1	0.4
Titanium oxide	–	46	53	0.3	0.2	0.03	1.0
Titanium	–	76	23	0.01	0.01	0.04	0.9

<sup>a)</sup>Hydrogen cannot be unambiguously attributed to residual gases in the analysis chamber or originating from the specimen.

isotope distribution of titanium. This causes the measured amount of phosphorous in the titanium oxide to be lower than the actual amount. In the chromium layer, a lower amount of calcium and phosphorus is found than in the titanium oxide. The Ca and P containing ions detected close to the interface can be attributed to hydroxyapatite particles, as the particle layer is seen to be up to 30 nm thick in the TEM micrographs. The detected amounts of Ca and P species in the chromium layer can partly also be attributed to overlaps in the mass spectrum due to thermal tails of the chromium oxide peaks. Hydrogen is detected in a higher amount in the titanium oxide and the titanium compared to the chromium. This can be explained by either the higher field required to maintain the evaporation rate causing a higher amount of residual gas hydrogen to be adsorbed to the specimen,<sup>[35]</sup> or that it is originating from the sample rather than residue gases in the analysis chamber as titanium is known to pick up hydrogen.<sup>[36]</sup> This could then be attributed to both the presence of hydrogen in the hydroxyapatite and in the titanium.

The APT data analysis proved to be challenging due to the high number of peaks in the mass spectrum. The hydroxyapatite evaporates in various molecular species, other studies report several peaks in the range 10–50 Da as nanoHA related<sup>[27]</sup> while the chemically similar bone is reported to evaporate as many different ions with varying mass-to-charge-state ratios.<sup>[37]</sup> Numerous of these overlap with the different molecular species attributed to the chromium and titanium oxides. However, in the range 39–46 Da there are peaks that in the titanium oxide region cannot be attributed to any titanium-related ions, instead they are identified as hydroxyapatite related, such as  $\text{PO}_3^{2+}$ ,  $\text{PO}_3\text{H}^{2+}$ ,  $\text{PO}_3\text{H}_2^{2+}$ ,  $\text{PO}_3\text{H}_3^{2+}$ ,  $\text{CaO}_3^{2+}$ , and  $\text{CaO}_3\text{H}_2^{2+}$ , which are used to assess the hydroxyapatite content in the oxide. A  $\text{TiO}_2^{2+}$  signal is possible at 40 Da, but the isotope distribution of titanium makes it impossible for such a signal to explain the majority of the ions detected at for example 39.5 and 40.5 Da. Due to the ambiguous mass spectrum, the exact calcium and phosphorous content in the titanium oxide is difficult to determine, but their presence in the oxide can be verified, confirming that the atoms of the nanoHA particle material partly diffuse into the underlying substrate. This likely occurs during the calcination step of the coating process.

In analysis of the reconstructed APT data, it is of interest to study the diffusion profile of Ca and P in the titanium/titania substrate. By making a 1D-concentration profile, as shown in **Figure 7**, the amount of calcium and phosphorous throughout the layer could be investigated. It should be noted in the concentration profile that the mass spectrum ranged for the entire specimen is applied, compared to the region-specific mass spectrum ranges used to measure the content in Table 1.

In a previous study, where the interface between bone and an implant was analyzed with APT after 4 weeks of healing, a calcium-enriched region was found on the outer surface of the implant.<sup>[22]</sup> This was not observed in the material analyzed in this study. Instead, the amounts of calcium and phosphorus detected throughout the titanium oxide layer were relatively constant, as shown in **Figure 7c**. In the aforementioned study, the calcium enrichment is attributed to the positive calcium ions having an affinity to the slightly negative oxide scale of the titanium, and the smaller phosphorous atoms also diffuse more easily in

the material. In this work, however, the heat treatment provides enough energy for both calcium and phosphorous to diffuse through the entire oxide.

As shown in **Figure 7c**, the carbon content follows the calcium and phosphorous content; this is due to nanoHA prepared in solution forms carbonated hydroxyapatite, where some of the phosphate is substituted with carbonate.<sup>[33]</sup> The measured carbon content by APT is significantly lower than by EDX (Table S1, Supporting Information), explained by lack of contamination of the sample as well as the lower reliability when measuring lower atomic weight elements by EDX. Here, APT gives a more reasonable estimate of the carbon content in the nanoHA. As the measured carbon content is lower in the chromium layer, it is not attributed to the sputter coating, nor the use of GIS-deposited platinum during the FIB specimen preparation.

In the reconstructed data above, the ratio of Ca:P is close to 1:1, which disagrees with the observed ratios in the EDX data. This can partly be explained by loss of ions due to the mentioned overlaps in the APT mass spectrum. If the evaporation field of calcium is lower than the field for the materials in the matrix, preferential evaporation of calcium between the laser pulses can occur.<sup>[38]</sup> The laser energy used above was 65 pJ, when increased to 95 pJ the detected amount of calcium and phosphorous increased, as shown in **Figure 8** and **Table 2**, suggesting that this can be the case. The mass spectra from the boxes in **Figure 8b** can be found in **Figure S12**, Supporting Information.

The data from the second reconstructed specimen show a Ca:P ratio in the titanium oxide higher than the ones obtained by EDX (1.33–1.47) and the theoretical ratio based on the stoichiometric composition of hydroxyapatite (1.67). In bone; however, the mineral is often observed to be calcium deficient, showing values ranging between 1.2 and 1.5<sup>[39]</sup> and similar deficiency can be expected for synthetic rod-shaped hydroxyapatite.<sup>[17]</sup> The higher calcium amount measured using the higher laser energy can tentatively be explained by less preferential evaporation while more of the phosphorous is still lost. The measured quantities are still significantly lower than obtained by EDX quantification (Table S1, Supporting Information), indicating that the peaks identified as unambiguously hydroxyapatite related do not cover all the evaporated ions but rather that a large amount of them have the same mass-charge ratio as species identified as chromium or titanium related and consequently cause overlaps in the mass spectrum or are evaporated between the laser pulses. The ratio of oxygen to titanium, as measured by APT, is found to be lower than that determined by EDX. This aligns with the typically observed underestimation of oxygen content in APT measurements of oxides.<sup>[40]</sup> Further, it is observed that the amount of detected oxygen within the titanium decreases when higher laser energy is employed during the APT process. This observation is also consistent with the phenomenon of underestimating oxygen levels.<sup>[41]</sup> The measured hydrogen is higher in the titanium region, while the relative charge state ratios of TiO between the titanium region and titanium oxide region suggests that the field is higher in the titanium oxide region. This suggests that the hydrogen at least partly originates from the specimen rather than residual gases in the analysis chamber.

Similarly, as in the first reconstruction, a 1D concentration profile can be made to closer investigate the diffusion profile



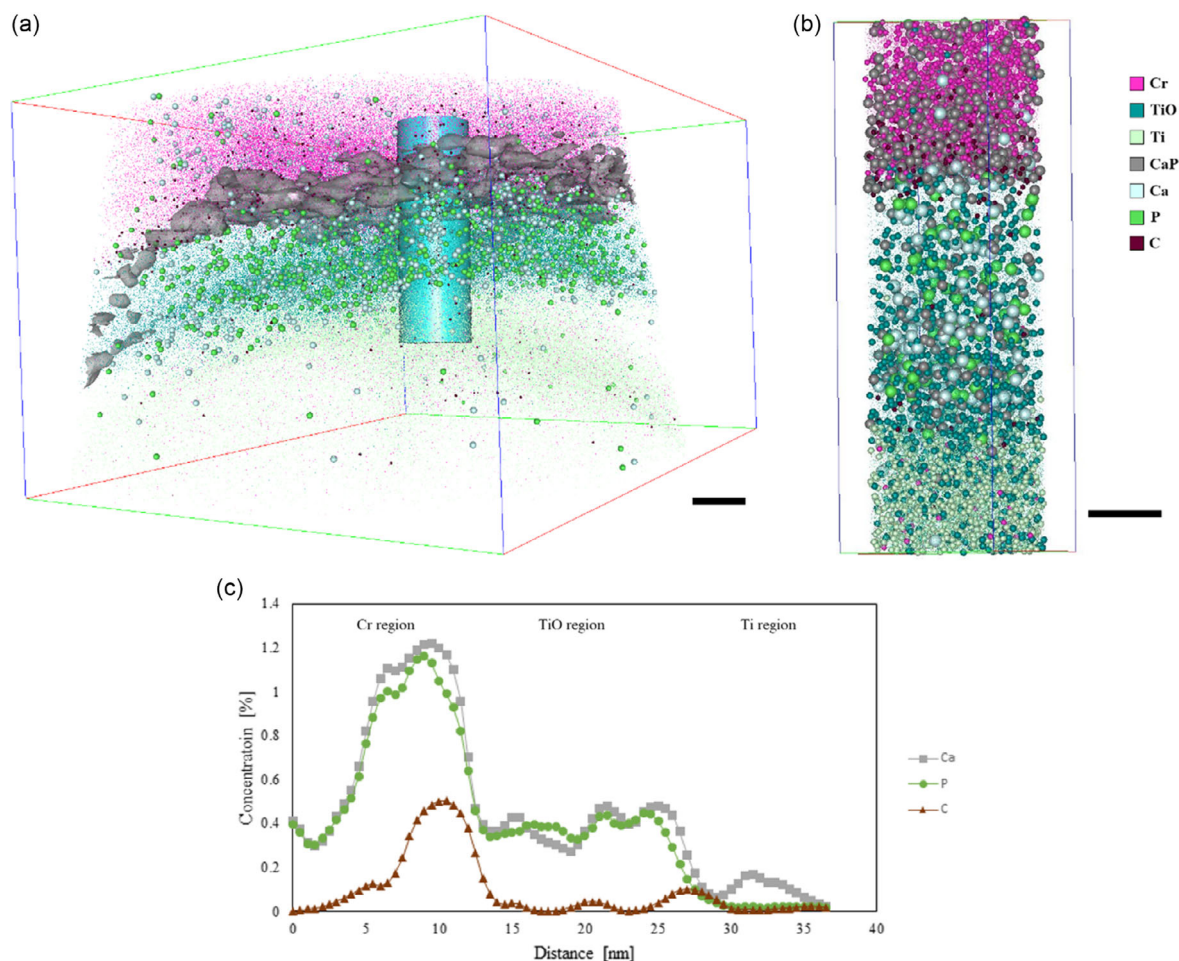


**Figure 7.** a) Region surrounding titanium surface oxide layer from a reconstructed APT analysis. Calcium and phosphorous are highlighted; the gray isosurface highlights CaP (71 Da) at 1.75%. The cylinder is used to measure the Ca and P content. Scale bar: 10 nm. b) Content of the cylinder highlighted in (a). Scale bar: 5 nm. The species highlighted as Ca is the  $\text{CaO}_3^{2+}$  peak at 44 Da and the species highlighted as P is the  $\text{PO}_3\text{H}_2^{2+}$  peak at 40.5 Da. c) 1D concentration profile of the Ca, P, and C content in (b).

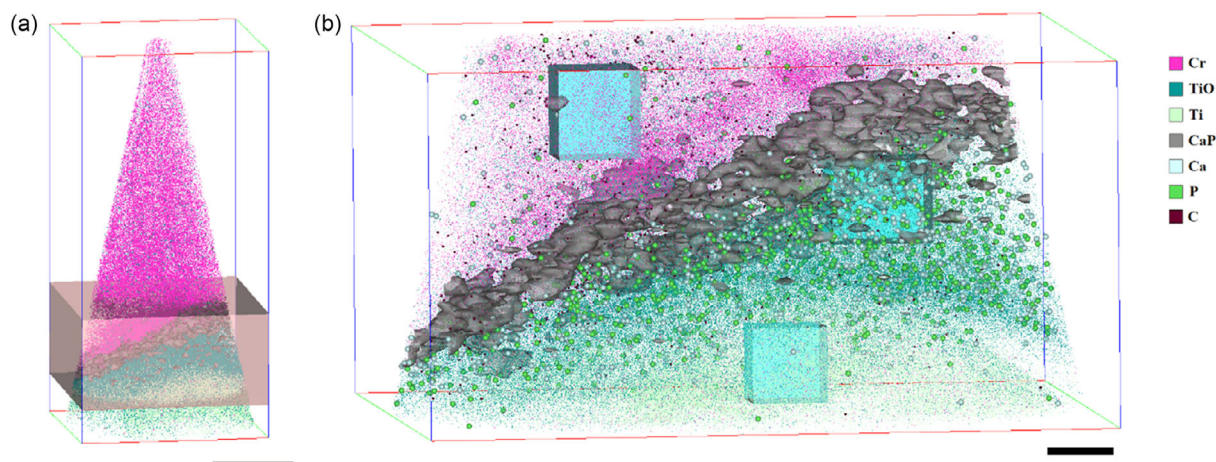


**Figure 8.** a) Reconstructed APT data from specimen analyzed with the laser energy at 95 pJ. An isosurface set at 2% CaP (71 Da) is in gray. Scale bar: 50 nm. b) Analysis of the region highlighted with a box in (a). The three sub-boxes were used to analyze the composition of the chromium, titanium oxide, and titanium, respectively. The species highlighted as Ca is the  $\text{CaO}_3^{2+}$  peak at 44 Da and the species highlighted as P is the  $\text{PO}_3\text{H}_2^{2+}$  peak at 40.5 Da. Scale bar: 10 nm.



**Table 2.** Measured bulk composition (atomic %) of the different regions highlighted in Figure 8b, obtained by mass spectrum analysis of the reconstructed APT data.

Region	Cr	Ti	O	Ca	P	C	H <sup>a)</sup>
Chromium	71	–	28	0.2	0.2	0.01	0.03
Titanium oxide	–	45	53	0.6	0.3	0.1	0.9
Titanium	–	86	13	0.01	0.01	0.01	1.6

<sup>a)</sup>Hydrogen cannot be unambiguously attributed to residual gases in the analysis chamber or originating from the specimen.

of the Ca and P in the titanium oxide layer, as shown in Figure 9. The carbon is following the same trend as in the previous specimen, where it follows the calcium and phosphorous profile. Here, carbon is also detected throughout the titanium oxide, suggesting that some diffusion of the carbon from the carbonated hydroxyapatite also occurs. As in the lower laser energy analysis, the lack of measured carbon in the chromium and titanium layers indicates that the carbon is not a result of the sputtering process or the specimen preparation.

As shown in Table 2, the detected Ca and P in the TiO region are higher than in the first analyzed specimen and the Ca:P ratio is also higher, especially further down in the layer. The measured calcium concentration is low relative to titanium, ruling out the formation of an intermediate phase rather than traces of calcium in the titanium oxide structure. In the Cr region, the Ca:P ratio is closer to one, indicating that the evaporation of nanoHA as CaP at 71 Da has a significant contribution to the detected calcium and phosphorous.

The APT results confirm the presence of calcium and phosphorous in the titanium surface oxide, which aligns with the findings from the EDX measurement. However, it is important to consider the challenges of quantitative analysis when studying low concentration elements at nanoscale material features. The EDX measurement may encounter challenges due to the generation of X-rays outside the studied region, as well as its unreliability in measuring low atomic weight elements. In contrast, the APT measurement offers a higher spatial resolution, enhancing the credibility of observing elements in specific regions. Nonetheless, quantitative analysis remains challenging due to factors such as preferential evaporation, underestimation of oxygen, and overlaps in the mass spectrum. Despite these challenges, the results provide evidence of the presence of the

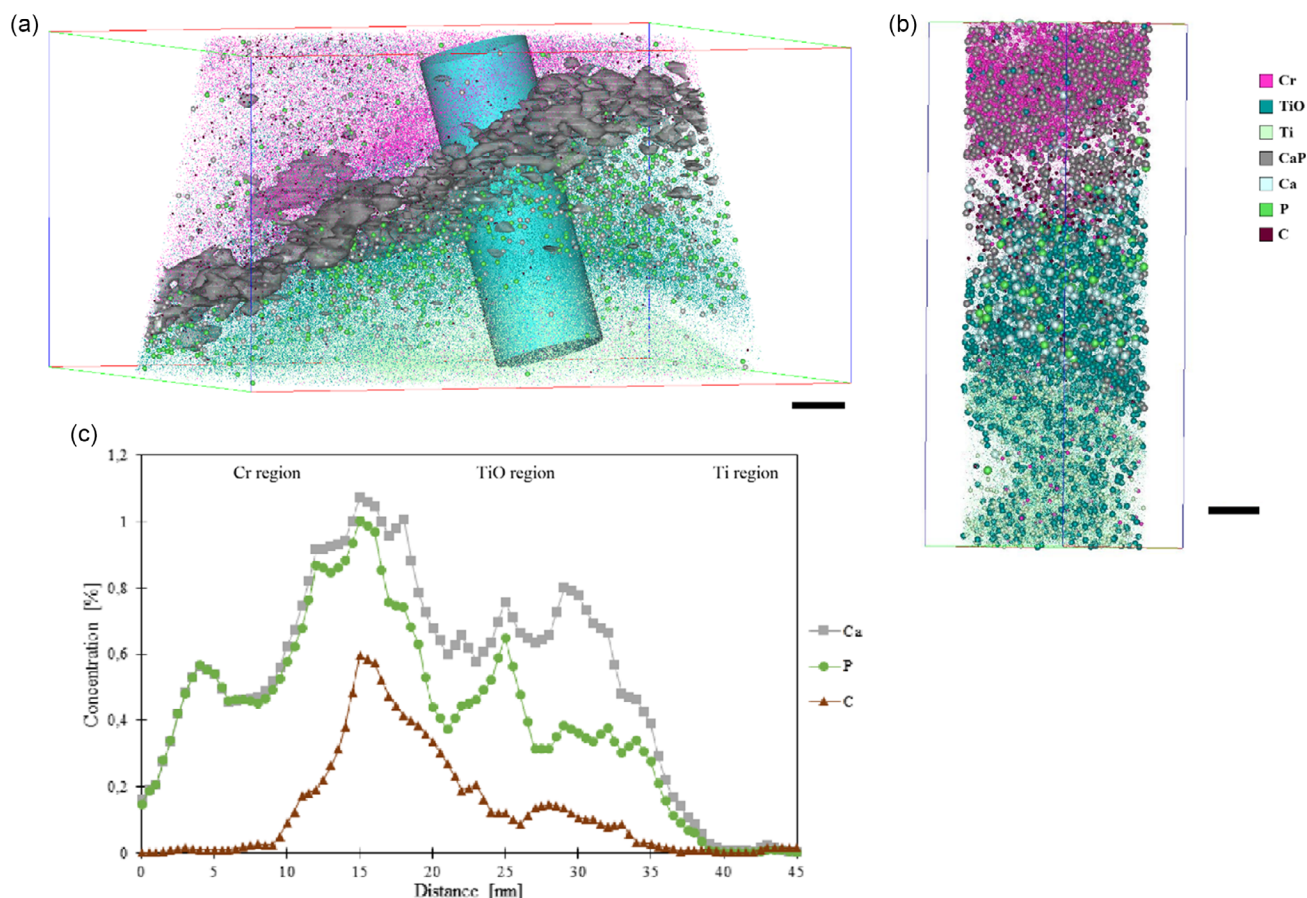


**Figure 9.** a) Region surrounding titanium surface oxide layer from a reconstructed APT analysis. Calcium and phosphorous are highlighted; the gray isosurface highlights CaP (71 Da) at 2%. The cylinder is used to measure the Ca and P content. Scale bar: 10 nm. b) Content of the cylinder highlighted in (a). Scale bar: 5 nm. The species highlighted as Ca is the  $\text{CaO}_3^{2+}$  peak at 44 Da and the species highlighted as P is the  $\text{PO}_3\text{H}_2^{2+}$  peak at 40.5 Da. c) 1D concentration profile of the Ca, P, and C content in (b).

elements of interest in the titanium oxide, with an approximate concentration of a few atomic %.

The detection of calcium and phosphorus in the titanium surface oxide of the investigated materials indicates the potential for achieving a resemblance of osseointegration at the atomic scale even before the utilization of a medical device. These materials hold promise for improving success rates, expediting the healing process, and mitigating the risk of implant-related infections. The widespread adoption of such materials could significantly reduce costs and alleviate the suffering associated with numerous routine medical procedures worldwide. Moreover, this study demonstrates the suitability of sputter-coated chromium on a nanostructured titanium surface for APT analysis. Analyzing multilayered materials often poses challenges in APT, but here, the moderately rough topography of the titanium surface, coupled with the compatible evaporation field of chromium, renders it an effective material for analysis under diverse experimental conditions. Despite encountering certain obstacles arising from the presence of oxide layers on metals and their numerous isotopes, particles deposited on the surface can still be investigated, albeit with limitations due to the mass spectrum containing numerous peaks originating from the matrix, which may overlap with the desired material of interest. This discovery paves the way for potential APT analysis of other previously elusive materials through the process of nanostructuring titanium surfaces and subsequently embedding them with chromium.

## 4. Conclusions

We have achieved a near-atomically resolved analysis and reconstruction of hydroxyapatite nanoparticles on titanium implant surfaces using APT. Our findings demonstrate that calcium and phosphorus from these nanoparticles diffuse into the surface oxide of the titanium implant material during the manufacturing process.

By pretreating the sample with a thin sputter-coated chromium film, the construct remained stable throughout the APT analysis, although multilayered materials often present challenges in APT analyses.

These results provide valuable insights for the development of next generation of osseointegrating implants as well as providing a tool for analyzing multilayered materials and nanomodified surfaces using APT.

## Supporting Information

Supporting Information is available from the Wiley Online Library or from the author.

## Acknowledgements

Promimic AB is acknowledged for providing the nanoHA-coated titanium samples. This work was funded by the Knut and Alice Wallenberg Foundation, KAW. This work was performed in part at the Chalmers Material Analysis Laboratory, CMAL. Dr. Constantinos Hatzoglou and Dr. Paraskevas Kontis at the Norwegian University of Science and Technology, NTNU, are thanked for their assistance with APT analysis.

## Conflict of Interest

The authors declare no conflict of interest.

## Data Availability Statement

The data that support the findings of this study are available from the corresponding author upon reasonable request.

## Keywords

atom probe tomography, hydroxyapatite, integration, nanoparticles, titanium, transmission electron microscopy

Received: May 11, 2023

Revised: August 4, 2023

Published online:

- [1] V. R. Sastri, in *Plastics in Medical Devices*, 3rd ed. (Ed: V. R. Sastri), Elsevier, Oxford **2022**, pp. 1–11.
- [2] P. S. Stewart, T. Bjarnsholt, *Clin. Microbiol. Infect.* **2020**, 26, 1034.
- [3] C. Kenney, S. Dick, J. Lea, J. Liu, N. A. Ebraheim, *J. Orthop.* **2019**, 16, 393.
- [4] W. Zimmerli, *J. Intern. Med.* **2014**, 276, 111.
- [5] P. I. Branemark, *J. Prosthet. Dent.* **1983**, 50, 399.
- [6] P. Tambasco De Oliveira, A. Nanci, *Biomaterials* **2004**, 25, 403.
- [7] L. Meirelles, A. Arvidsson, M. Andersson, P. Kjellin, T. Albrektsson, A. Wennerberg, *J. Biomed. Mater. Res. Part A* **2008**, 87, 299.
- [8] L. C. Junqueira, J. Carneiro, in *Basic Histology, Text & Atlas*, 10th ed. (Eds: J. Foltin, H. Lebowitz, P. J. Boyle), McGraw-Hill Companies, New York **2003**.
- [9] S. Awasthi, S. K. Pandey, E. Arunan, C. Srivastava, *J. Mater. Chem. B* **2021**, 9, 228.
- [10] Y.-P. Lu, M.-S. Li, S.-T. Li, Z.-G. Wang, R.-F. Zhu, *Biomaterials* **2004**, 25, 4393.
- [11] A. Jaafar, C. Hecker, P. Árki, Y. Joseph, *Bioengineering* **2020**, 7, 127.
- [12] F. Schönweger, C. M. Sprecher, S. Milz, C. Dommann-Scherrer, C. Meier, A. Dommann, A. Neels, P. Wahl, *Materials* **2020**, 13, 4713.
- [13] G. Graziani, M. Berni, A. Gambardella, M. De Carolis, M. C. Maltarello, M. Boi, G. Carnevale, M. Bianchi, *Mater. Sci. Eng. C* **2019**, 99, 853.
- [14] W. Suchanek, M. Yoshimura, *J. Mater. Res.* **1998**, 13, 94.
- [15] R. Z. LeGeros, *Chem. Rev.* **2008**, 108, 4742.
- [16] A. Lotsari, A. K. Rajasekharan, M. Halvarsson, M. Andersson, *Nat. Commun.* **2018**, 9, 4170.
- [17] E. Westas, M. Gillstedt, J. Lönn-Stensrud, E. Bruzell, M. Andersson, *J. Biomed. Mater. Res. Part A* **2014**, 102, 1063.
- [18] C. Han, Y. Li, Q. Wang, D. Cai, Q. Wei, L. Yang, S. Wen, J. Liu, Y. Shi, *Mater. Des.* **2018**, 141, 256.
- [19] A. Arifin, A. B. Sulong, N. Muhamad, J. Syarif, M. I. Ramli, *Mater. Des.* **2014**, 55, 165.
- [20] A. Y. Berezhnaya, V. O. Mittova, A. V. Kostyuchenko, I. Y. Mittova, *Inorg. Mater.* **2008**, 44, 1214.
- [21] J. S. Kim, S. M. Kang, K. W. Seo, K. Y. Nahm, K. R. Chung, S. H. Kim, J. P. Ahn, *Biomed. Res. Int.* **2015**, 2015, 960410.
- [22] J. Karlsson, G. Sundell, M. Thuvander, M. Andersson, *Nano Lett.* **2014**, 14, 4220.
- [23] G. Sundell, C. Dahlin, M. Andersson, M. Thuvander, *Acta Biomater.* **2017**, 48, 445.
- [24] M. K. Miller, *Microsc. Microanal.* **2004**, 10, 150.

- [25] K. Grandfield, C. Micheletti, J. Deering, G. Arcuri, T. Tang, B. Langelier, *Acta Biomater.* **2022**, *148*, 44.
- [26] P. Felfer, T. Li, K. Eder, H. Galinski, A. P. Magyar, D. C. Bell, G. D. W. Smith, N. Kruse, S. P. Ringer, J. M. Cairney, *Ultramicroscopy* **2015**, *159*, 413.
- [27] D. S. Mosiman, Y. S. Chen, L. Yang, B. Hawket, S. P. Ringer, B. J. Mariñas, J. M. Cairney, *Small Methods* **2021**, *5*, 2000692.
- [28] B. W. Kempshall, L. A. Giannuzzi, B. I. Prenitzer, F. A. Stevie, S. X. Da, *J. Vac. Sci. Technol. B: Microelectron. Nanometer Struct.* **2002**, *20*, 286.
- [29] R. M. Langford, C. Clinton, *Micron* **2004**, *35*, 607.
- [30] L. A. Giannuzzi, F. A. Stevie, *Micron* **1999**, *30*, 197.
- [31] J. Hernández-Saz, M. Herrera, S. I. Molina, *Micron* **2012**, *43*, 643.
- [32] J. H. Bunton, J. D. Olson, D. R. Lenz, T. F. Kelly, *Microsc. Microanal.* **2007**, *13*, 418.
- [33] E. Landi, G. Celotti, G. Logroscino, A. Tampieri, *J. Eur. Ceram. Soc.* **2003**, *23*, 2931.
- [34] T. T. Tsong, *Surf. Sci.* **1978**, *70*, 211.
- [35] G. Sundell, M. Thuvander, H. O. Andrén, *Ultramicroscopy* **2013**, *132*, 285.
- [36] Y. Zhu, T. W. Heo, J. N. Rodriguez, P. K. Weber, R. Shi, B. J. Baer, F. F. Morgado, S. Antonov, K. E. Kweon, E. B. Watkins, D. J. Savage, *Curr. Opin. Solid State Mater. Sci.* **2022**, *26*, 101020.
- [37] B. Langelier, X. Wang, K. Grandfield, *Sci. Rep.* **2017**, *7*, 39958.
- [38] C. Hatzoglou, S. Rouland, B. Radiguet, A. Etienne, G. D. Costa, X. Sauvage, P. Pareige, F. Vurpillot, *Microsc. Microanal.* **2020**, *26*, 689.
- [39] M. Glimcher, *Rev. Mineral. Geochem.* **2006**, *64*, 223.
- [40] M. Bachhav, F. Danoix, B. Hannoyer, J. M. Bassat, R. Danoix, *Int. J. Mass Spectrom.* **2013**, *335*, 57.
- [41] N. Amirifar, R. Lardé, E. Talbot, P. Pareige, L. Rigutti, L. Mancini, J. Houard, C. Castro, V. Sallet, E. Zehani, S. Hassani, *J. Appl. Phys.* **2015**, *118*, 215703.